Journal of The Electrochemical Society, **156** (10) B1134-B1141 (2009)
0013-4651/2009/156(10)/B1134/8/$25.00 © The Electrochemical Society

Porous-Media Flow Fields for Polymer Electrolyte Fuel Cells
II. Analysis of Channel Two-Phase Flow

Yun Wang[*,z]

Renewable Energy Resources Laboratory and National Fuel Cell Research Center, Department of Mechanical and Aerospace Engineering, The University of California, Irvine, Irvine, California 92697-3975, USA

Following the concept developed in Part I of this study [Y. Wang, *J. Electrochem. Soc.*, **156**, B1124 (2009)], this paper deals with the two-phase transport in the porous-media channel for polymer electrolyte fuel cells (PEFCs). Two-phase flow in the channel plays a crucial role in both reactant supply and water removal for a high humidity operation. Based on the two-fluid description, we developed a two-phase transport model for the PEFC channel, and we further analytically obtained the profiles of the phase velocities, liquid/gas volume fractions, and pressures for both liquid and gas phases along the channel. We find that the impact of the capillary action can be neglected for the liquid transport along the channel. The prediction of liquid saturation profiles varies considerably when using different models of the relative permeabilities. A maximum liquid saturation of approximately 20% is predicted, which avoids the occurrence of a high transport resistance for gaseous reactants. Pores in the porous-media channel cannot be completely occupied by liquid due to the dominant interfacial forces among the phases. These benefits make the proposed porous channel approach superior to the traditional hollow channels in terms of two-phase transport characteristics.
 [DOI: 10.1149/1.3183785]

Manuscript submitted April 9, 2009; revised manuscript received June 23, 2009. Published July 31, 2009.

The reactant channel of polymer electrolyte fuel cells (PEFCs) plays a crucial role in fuel cell operation. It supplies the gaseous reactants and removes product water for fuel cells. At a high humidity operation, fuel cells are frequently subjected to flooding; i.e., produced water condenses to liquid water, and channel flows are featured by the liquid-reactant gas transport (see Fig. 1). As liquid may block the channel and the diffusion passages toward the catalyst layer, the characteristics of a two-phase transport may significantly affect the fuel cell performance. Issues such as local reactant starvations arising from flooding may be linked to cell degradation.

Several experiments have revealed complex two-phase phenomena in fuel cells.[1-4] To date, most efforts are devoted to modeling the two-phase flow in the gas diffusion layer (GDL) and the catalyst layer.[5-24] Early two-phase models include those of Wang et al.,[5] Natarajan and Nguyen,[8] Rowe and Li,[16] and You and Liu.[17] Recently, Nam and Kaviany[6] explored the influences of the fiber diameter, porosity, and capillary pressure on the liquid water removal in the cathode. Pasaogullari and Wang conducted a one-dimensional (1D) analysis of the liquid saturation profile across the GDL.[7] Yuan and Sunden[18] presented a multidimensional model to describe the two-phase phenomena in fuel cells. Costamagna[19] also developed a multidimensional model but neglected the phase change heat. Berning and Djlali[20] presented a two-phase model based on the unsaturated flow theory for two-phase flow in porous media, which assumes a constant gas-phase pressure across the medium, and the capillary action plays a dominant role. The model of Mazumder and Cole[9] was developed for hydrophilic GDLs and was based on the M2 model,[21] which is primarily for a dispersion two-phase system. The M2 model treats the liquid and gas phases as a mixture and describes the conservation of individual components in all the phases. Other models adopting the M2 approach include Hu et al.,[22] Wang and Wang,[14,15] Luo et al.,[23] and Wang.[24] Birgersson et al.[12] presented a two-fluid flow model consisting of separate equations for water transport in liquid and gas phases, respectively. Phase interactions are described by a source term in the equations. In most of the studies, the two-phase model in GDLs is also extended to the porous electrode. Wang and Feng[25] indicated that the liquid saturation through-plane profile varied little ($<5\%$) in the cathode.

Reactant transport in channels is included in most of the previous fuel cell models. However, the majority only consider a single-phase flow, while few approaches deal with a two-phase transport or flooding in channels, which frequently occurs at a high humidity operation. Several visualizations indicate the occurrence of the channel flooding in fuel cells.[1-4] Yuan and Sunden[18] tried the channel two-phase flow model, employing a one-fluid model. Hu et al.[22] applied the M2 description to the channel and GDL regions. Wang et al.[26] also considered the M2 description in their study. However, using the dispersion model to describe the channel flooding raises concerns that two-phase flows in hollow microchannels typically exhibit several patterns and that some of them may not be well described by a dispersion model (see Fig. 1).

An approach to PEFC channel design was proposed recently,[27] in which porous media are adopted in the channel region, allowing transport of electrons and heat directly across the channel region. We studied a low humidity operation of PEFCs with this type of PEFC channel in the previous study.[27] The objective of this paper is to further the discussion to a two-phase region and to investigate the characteristics of the two-phase flow for this approach. We started with a two-fluid model and analyzed the two-phase flow within the porous-media channel. The profiles of the important quantities of two-phase flows were analytically obtained. Results demonstrate the superior characteristics of the two-phase transport in the porous-media channel.

Two-Phase Model in the Channel

Figure 2 schematically shows a cross section of the porous-media channel and the two-phase flows within. Based on the analysis in Ref. 27, a porous medium with pore sizes of 20–100 μm and porosities of 0.9–0.95 can ensure a sufficient flow conductance (including negligible pumping power). At a high humidity operation,

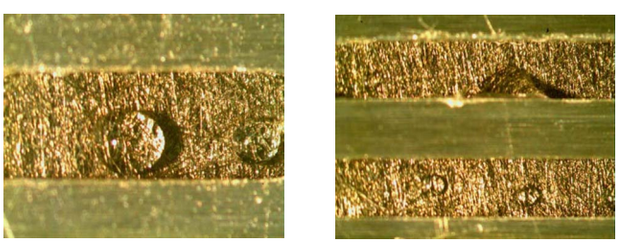

(a) (b)

Figure 1. (Color online) Visualization of the two-phase flow inside a hollow channel in the PEFC cathode: (a) Droplets in a channel. (b) Droplets in the lower channel and droplet attaching the channel wall in the upper channel. The channel cross-section dimension is 1 × 1 mm.

* Electrochemical Society Active Member.
[z] E-mail: yunw@uci.edu

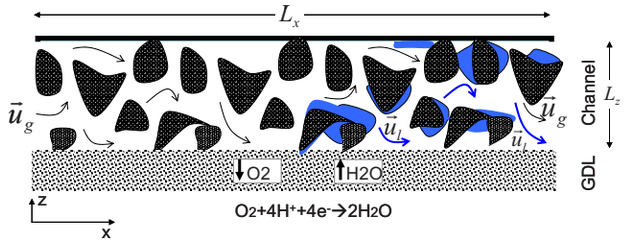

Figure 2. (Color online) The two-phase flow within the porous-media channel in the PEFC cathode.

partially or fully humidified reactants are injected into the channel. The reactants transport through the interconnected pore structure, with part of the mass diffusing toward the catalyst layer for the reaction (see Fig. 2). Simultaneously, water is produced and added to the channel flow. Liquid emerges when the gas relative humidity (RH) reaches unity, leading to a two-phase transport in the porous channel. Cold start typically operates at high humidity due to the low temperature. In that case, ice instead of liquid water emerges. The analysis[28] indicates that the channel region can only remove a small portion of the produced water. The solid water may also deposit on the surface of the solid matrix, instead of traveling with the gas flow forming a gas–solid transport. Therefore, we exclude our discussion on the cold start operation.

The two-fluid flow model.— The liquid-gas flow in the channel is transported in the interconnected pore structure of the porous media. The mass exchange occurs at the phase interface during water evaporation or condensation. The mass conservation of each phase can be written as follows

$$\text{Gas-phase mass conservation:} \quad \nabla \cdot (\rho_g \mathbf{u}_g) = S_m^{fg} \qquad [1]$$

$$\text{Liquid-phase mass conservation:} \quad \nabla \cdot (\rho_l \mathbf{u}_l) = -S_m^{fg} \qquad [2]$$

where $\mathbf{u}_g$ and $\mathbf{u}_l$ are the superficial velocities of gas and liquid, respectively. The gas density can be calculated through the constituent species

$$\rho_g = \sum_k M_k C_k \qquad [3]$$

Here, k represents species. The cathode species include nitrogen, water, and oxygen.

Flow in the porous media is driven by the pressure gradient and body forces and balanced with the shear stress at the solid surface. A dimensionless number, Bond (Bo), is usually defined to compare the body force with the surface tension, $Bo = (g\Delta\rho/\sigma)L_p^2$, where $\Delta\rho$, L_p, g, and σ are the density difference between phases, the pore diameter, the gravity, and the surface tension, respectively. For a water–air two-phase system and $L_p \sim 50$ μm, $Bo < 0.001$; therefore, the influence of the gravitational force can be neglected. By adopting Darcy's law, the momentum equations can be written as

$$\text{Gas-phase momentum conservation:} \quad \rho_g \mathbf{u}_g = -\frac{k_{rg} K}{\nu_g} \nabla P_g \qquad [4]$$

$$\text{Liquid-phase momentum conservation:} \quad \rho_l \mathbf{u}_l = -\frac{k_{rl} K}{\nu_l} \nabla P_l \qquad [5]$$

The relative permeabilities, k_{rg} and k_{rl}, are defined as the ratio of the intrinsic permeability of the liquid/gas phase to the total permeability of a porous medium. Physically, it describes the extent to which one fluid is hindered by others in pore spaces and can be approximated as a function of liquid saturation. The relative permeability may also depend on other parameters including residual saturation and interfacial area, as suggested by Hilfer.[29] A set of functions has been used in the fuel cell literature for the relative permeabilities

$$k_{rl} = s_e^{n_k} \quad \text{and} \quad k_{rg} = (1 - s_e)^{n_k} \quad \text{where the effective saturation}$$

$$s_e = \frac{s_l - s_{ir}}{1 - s_{ir}} \qquad [6]$$

n_k of unity, i.e., a linear relationship between k and s, is called the X-curve model,[30] the simplest expression for the relative permeability. In fuel cells, most studies adopted the value of either 3 or 4 for the exponent.[7,14-16] The larger n_k is, the greater the degree to which the liquid water affects the gas flow. The irreducible residual saturation, s_{ir}, is physically the liquid fraction bound inside the capillary channel by surface tension force and hence cannot be removed by drainage but only by evaporation. Physically, it may be caused by the fact that the wetting liquid is disconnected or exists in isolated spots in the media. It may also be associated with the local heterogeneity that part of the media characterized by pore dimensions is considerably lower than that of the rest of the media.[31]

Corey[32] suggested a formula similar to Eq. 6 with k_{rl} having $n_k = 4$ while k_{rg} reads

$$k_{rg} = (1 - s_e)^2(1 - s_e^2) \qquad [7]$$

Fourar and Lenormand[30] proposed another expression considering the impact of the fluid viscosities[33]

$$k_{rl} = \frac{s_l^2}{2}(3 - s_l) \quad \text{and} \quad k_{rg} = (1 - s_l)^3 + \frac{3}{2}\frac{\mu_g}{\mu_l} s_l (1 - s_l)(2 - s_l) \qquad [8]$$

In Eq. 5, the liquid pressure P_l is defined as the difference between the gas and the capillary pressures, i.e., $P_g - P_c$. Leverett suggested the J-function for the drainage capillary pressure that can be approximated by a function of surface properties such as surface tension σ and contact angle θ_c, porous-medium properties such as porosity ε and permeability K, and the liquid saturation s_l

$$P_c = \sigma \cos(\theta_c)\left(\frac{\varepsilon}{K}\right)^{1/2} J(s_l) \qquad [9]$$

The above takes the effects of interfacial tension into account but fails to consider the tortuous nature of a porous media. In the above equation, $J(s_l)$ is the Leverett function, an empirical relation that is frequently adopted for both hydrophobic and hydrophilic porous media

$$J(s_l) = \begin{cases} 1.417(1 - s_l) - 2.120(1 - s_l)^2 + 1.263(1 - s_l)^3 & \text{for } \theta_c < 90^\circ \\ 1.417 s_l - 2.120 s_l^2 + 1.263 s_l^3 & \text{for } \theta_c > 90^\circ \end{cases} \qquad [10]$$

The Leverett function is usually for the packed bed such as unconsolidated sands. For other structures of the porous-media channel, e.g., porous metal or carbon-fiber-based porous media, the above equation may be a source of inaccuracy.

Materials for porous-media channels can be hydrophilic, e.g., metals or carbon. The hydrophilic media are beneficial for the GDL liquid removal. It is also possible to adopt the hydrophobic channels,

as long as the liquid water removal in the GDL is not prohibited, which is determined by the balance of the capillary forces at the GDL–channel interface.

Water transport.— Water is a by-product of the electrochemical reaction occurring in the cathode of fuel cells (see Fig. 2). In addition to reaction production, the electro-osmotic drag also contributes water addition in the cathode. Part of the water returns to the anode by back-diffusion. A parameter, named the net water transport coefficient, can be introduced to account for the combined effects of the electro-osmotic drag and back-diffusion. Within the cathode catalyst layer, water is added at the location of the triple-phase boundaries and enters the thin ionomer film, attaching the sulfonic groups. Excessive water in the ionomer moves to the electrode pores and is further delivered to the channel region via the GDL in either gas or liquid phase. The water flux at the channel–GDL interface is described in the section of boundary conditions. In the channel region, water transport takes place in either gas or liquid phase. Note that the liquid is purely water. One can derive the water conservation as

Water conservation:

$$\nabla \cdot \left(\mathbf{u}_g C_g^{H_2O} + \mathbf{u}_l \frac{\rho_l}{M^{H_2O}} \right) = \nabla \cdot (\varepsilon s_g D_g^{H_2O} \nabla C_g^{H_2O}) \quad [11]$$

The above transport equation considers two mechanisms of species transport, i.e., convection and diffusion. The effect of the capillary action is also contained [in the liquid velocity (see Eq. 5]. In the gas phase, the species diffusion coefficient in Eq. 11 is given by

$$D_g^k = D_{g,o}^k \left(\frac{T}{353} \right)^{3/2} \left(\frac{1}{p} \right) \quad [12]$$

Boundary conditions.— Equations 1, 2, 4, 5, and 11 form a set of governing equations, with $\mathbf{u}_g$, $\mathbf{u}_l$, P_g, P_l, and $C_g^{H_2O}$ as the unknowns, to describe two-phase flow and water transport. In the following, we only explain the associated boundary conditions unique to fuel cell porous-media channels.

Flow inlet boundaries. The cathode inlet flow is mostly partially or fully humidified before fed in. It is purely gas stream. The gas-phase inlet velocity, $\mathbf{u}_g$, is determined by the stoichiometric flow ratio, ξ_c, and the average current density, I

$$\mathbf{u}_g \cdot \mathbf{n}|_{inlet} = - \frac{I A_m}{F} \frac{\xi_c}{4 C_{g,in}^{O_2} A_c} \quad [13]$$

where A_c and A_m are the areas of flow cross sectional and the membrane, respectively. The inlet molar concentrations are determined by the inlet pressure and humidity according to the ideal gas law. Typically, no liquid is contained in the injected flow, i.e., $s_g = 1$ and $s_l = 0$.

Outlet boundaries. Fully developed or no-flux conditions are applied.

Solid walls. A no-slip and impermeable velocity condition and a no-flux condition are applied.

GDL–channel interface. As only the flow channel is considered, the GDL–channel interface becomes the boundary of the domain. Product water is injected into the channel at this interface. Meanwhile, oxygen transports out of the channel for the oxygen reduction reaction in the catalyst layer. By utilizing the net water transport coefficient α, one can express the water production and mass consumption rates via Faraday's law

$$S^{H_2O} = \frac{(1 + 2\alpha) I}{2F} \frac{A_m}{A_{ch}} \quad \text{and} \quad S_m = \left(\frac{1}{2} M^{H_2} + \alpha M^{H_2O} \right) \frac{A_m I}{A_{ch} F} \quad [14]$$

where A_m and A_{ch} represent the membrane area and channel projected area on the membrane, respectively. The mass added to the channel may be in liquid or gas phase. Assuming that a portion β of mass is in gas phase when entering the channel, the following boundary conditions can be developed by applying the interfacial flux relationship and water conservation

$$\rho_g \mathbf{u}_g \cdot \mathbf{n} = - \beta S_m \quad \rho_l \mathbf{u}_l \cdot \mathbf{n} = - (1 - \beta) S_m$$

$$C_g^{H_2O} \mathbf{u}_g \cdot \mathbf{n} - \varepsilon s_l D_g^{H_2O} \frac{\partial C_g^{H_2O}}{\partial n} + \frac{s_l \rho_l}{M^{H_2O}} \mathbf{u}_l \cdot \mathbf{n} = - S^{H_2O} \quad [15]$$

Analytical Solutions

The dimension along the channel is important as the reactant delivery and water removal in the channel primarily take place in this direction.[24] To simplify the analysis, we consider a single channel (either straight or serpentine) and assume that the quantities in the channel only vary in this dimension. Temperature is an important parameter in a two-phase transport. In fuel cell channels, its variation along the channel is typically controlled by the cooling unit and should usually be kept small to avoid component damage caused by nonuniform thermal expansion. In most nonisothermal studies (e.g., Ref. 14), temperature at the outer surface of the cathode bipolar plate is set uniform. Therefore, we assume an isothermal condition for the channel region.

Considering a 1D steady state, the boundary conditions of the mass conservation (Eq. 1 and 2) at the GDL–channel interface become a source term in the equation that can be rewritten as

$$L_z \frac{d \rho_g u_g}{dx} = S_m^{fg} + \beta S_m \quad [16]$$

$$L_z \frac{d \rho_l u_l}{dx} = - S_m^{fg} + (1 - \beta) S_m \quad [17]$$

where L_z denotes the channel depth and u_g and u_l represent the gas and liquid velocities, respectively, along the 1D channel. Likewise, the 1D water equation reads

$$L_z \frac{d}{dx} \left(\mathbf{u}_g C_g^{H_2O} + \mathbf{u}_l \frac{\rho_l}{M^{H_2O}} \right) = L_z \frac{d}{dx} \left(\varepsilon s_g D_g^{H_2O} \frac{d}{dx} C_g^{H_2O} \right) + S^{H_2O} \quad [18]$$

Single-phase transport.— When partially humidified air is injected, the channel stream is single phase at the initial stage. In the absence of liquid, S_m^{fg} is zero while β is 1 in Eq. 16. The integration of Eq. 16 from 0 to x yields

$$\rho_g u_g = \rho_{g,in} u_{g,in} + \frac{L_x}{L_z} \int_0^{\bar{x}} S_m(\hat{x}) d\hat{x} \quad [19]$$

where $\bar{x}$ $(=x/L_x)$ is the dimensionless distance from the inlet. ρ_g is determined by the content of each species within the gas. The dominant species in the air is nitrogen, which is inactive throughout the fuel cell. Assuming a constant gas density, the gas velocity can be obtained directly from Eq. 19. One can estimate the magnitude of the gas acceleration by considering that the whole channel is a single-phase regime

$$\frac{u_g - u_{g,in}}{u_{g,in}} = \frac{L_x \int_0^1 S_m d\hat{x}}{L_z \rho_g u_{g,in}} \quad [20]$$

which is small, approximately 5% at the operating condition of 1.0 A/cm^2 at 2 atm and $\alpha \sim 0.1$. Assuming a uniform current density I, the gas velocity can further be written as

$$\frac{u_g}{u_{g,in}} = 1 + \frac{4 C_{g,in}^{O_2}}{\rho_g \xi_c} \left(\frac{1}{2} M^{H_2} + \alpha M^{H_2O} \right) \bar{x} \quad [21]$$

Once the gas velocity is obtained, the gas pressure can be calculated directly from Darcy's law

$$P_g = P_{g,in} - L_x \int_0^{\bar{x}} \frac{\mu_g u_g}{K} d\hat{x} \quad [22]$$

The water vapor concentration can be obtained by substituting u_g to Eq. 18. One can further assume that convection dominates the water transport in channels, eliminating the diffusion term. Integration from 0 to $\bar{x}$ yields

$$C_g^{H_2O} = \frac{u_{g,in} C_{g,in}^{H_2O}}{u_g} + \frac{L_x \int_0^{\bar{x}} S^{H_2O} d\hat{x}}{u_g L_z} \quad [23]$$

Again, at a uniform current density, the above equations are simplified as

$$P_g = P_g(0) - \frac{\mu_g u_g(0) L_x}{K} \left[\bar{x} - 4 \left(\frac{1}{2} M^{H_2} + \alpha M^{H_2O} \right) \frac{C_{g,in}^{O_2}}{\rho_g \xi_c} \bar{x}^2 \right] \quad [24]$$

$$C_g^{H_2O} = \frac{C_{g,in}^{H_2O} + \frac{2(1+2\alpha) C_{g,in}^{O_2} \bar{x}}{\xi_c}}{1 + \frac{4 C_{g,in}^{O_2}}{\rho_g \xi_c} \left(\frac{1}{2} M^{H_2} + \alpha M^{H_2O} \right) \bar{x}} \quad [25]$$

Water concentration increases along the flow until the saturation value when liquid starts to form. The transition point $\bar{x}^*$ can be calculated by

$$\bar{x}^* = \left(\frac{\xi_c \rho_g}{2 C_{g,in}^{O_2}} \right) \frac{C_{g,sat}^{H_2O} - C_{g,in}^{H_2O}}{(1+2\alpha)\rho_g - 2 C_{g,sat}^{H_2O} \left(\frac{1}{2} M^{H_2} + \alpha M^{H_2O} \right)} \quad [26]$$

Two-phase transport.— At $\bar{x}^*$, liquid starts to form, leading to a two-phase transport. Similar to the single-phase flow analysis, one can integrate both mass conservation equations from $\bar{x}^*$ to $\bar{x}$

$$\rho_g u_g = \rho_g(\bar{x}^*) u_g(\bar{x}^*) + \frac{L_x}{L_z} \int_{\bar{x}^*}^{\bar{x}} (S_m^{fg} + \beta S_m) d\hat{x} \quad [27]$$

$$\rho_l u_l = \frac{L_x}{L_z} \int_{\bar{x}^*}^{\bar{x}} [-S_m^{fg} + (1-\beta) S_m] d\hat{x} \quad [28]$$

Applying the same integration over the water conservation equation yields

$$u_g C_g^{H_2O} + u_l \frac{\rho_l}{M^{H_2O}} = u_g(\bar{x}^*) C_{g,sat}^{H_2O} + \frac{L_x}{L_z} \int_{\bar{x}^*}^{\bar{x}} S^{H_2O} d\hat{x} \quad [29]$$

In the porous-media channel, liquid attaches on the surface of the solid matrix; therefore, the interfacial area between liquid and gas phases is large, and the equilibrium between liquid and gas phases holds true; i.e., $C_g^{H_2O}$ is equal to $C_{g,sat}^{H_2O}$. In the above equation, we also neglect the diffusion term due to this assumption. Again, assuming a constant gas density ρ_g, one can solve the phase superficial velocities

$$u_l = \frac{L_x M^{H_2O}}{L_z \rho_l (C_{g,sat}^{H_2O} M^{H_2O} - \rho_g)} \left(C_{g,sat}^{H_2O} \int_{\bar{x}^*}^{\bar{x}} S_m d\bar{x} - \rho_g \int_{\bar{x}^*}^{\bar{x}} S^{H_2O} d\hat{x} \right) \quad [30]$$

and

$$u_g = u_g(\bar{x}^*) - \frac{L_x}{L_z (C_{g,sat}^{H_2O} M^{H_2O} - \rho_g)} \left(\int_{\bar{x}^*}^{\bar{x}} S_m d\bar{x} - M^{H_2O} \int_{\bar{x}^*}^{\bar{x}} S^{H_2O} d\hat{x} \right) \quad [31]$$

Further, Darcy's laws for both phases can be written in one dimension as

$$u_g = -\frac{k_{rg} K}{\mu_g} \frac{dP_g}{dx} \quad [32]$$

$$u_l = -\frac{k_{rl} K}{\mu_l} \frac{dP_l}{dx} = -\frac{k_{rl} K}{\mu_l} \left(\frac{dP_g}{dx} - \frac{dP_c}{dx} \right) \quad [33]$$

Combining these two equations to eliminate dP_g/dx and then substituting Eq. 9 yield

$$u_l = \frac{\mu_g}{\mu_l} \frac{k_{rl}}{k_{rg}} u_g + \frac{k_{rl} (K\varepsilon)^{1/2} \sigma \cos(\theta_c)}{\mu_l L_x} \frac{dJ}{ds} \frac{ds_l}{d\bar{x}} \quad [34]$$

The above equation can be solved numerically. The liquid transport along the channel is primarily driven by the two-phase interaction through shear stress at the interface. Assuming that the capillary action is small and negligible, one can eliminate the derivative and obtain an algebraic equation. By considering Eq. 6, one can further explicitly solve the liquid saturation

$$s_l = \frac{\left(\frac{u_l \mu_l}{\mu_g u_g} \right)^{1/n_k} + s_{ir}}{1 + \left(\frac{u_l \mu_l}{\mu_g u_g} \right)^{1/n_k}} \quad [35]$$

The calculated saturation can be used to obtain the relative permeabilities and further the pressures through Darcy's laws

$$P_g = P_g(\bar{x}^*) - L_x \int_{\bar{x}^*}^{\bar{x}} \frac{\mu_g u_g}{k_{rg} K} d\hat{x} \quad [36]$$

$$P_l = P_g(\bar{x}^*) - L_x \int_{\bar{x}^*}^{\bar{x}} \frac{\mu_l u_l}{k_{rl} K} d\hat{x} \quad [37]$$

The total gas pressure drop through the porous channel is the sum of the ones in single and two-phase flows

$$\Delta \bar{P}_g = \frac{\Delta P_g}{\frac{\mu_g u_{g,in} L_x}{K}} = \int_0^{\bar{x}^*} \frac{u_g}{u_{g,in}} d\hat{x} + \int_{\bar{x}^*}^1 \frac{u_g}{u_{g,in}} \frac{1}{k_{rg}} d\hat{x} \quad [38]$$

Assuming a constant gas velocity in the channel, the scale of the pressure (i.e., the denominator in the middle term of the above equation) becomes the pressure drop for a single-phase flow. The above equation can further be rearranged as

$$\Delta \bar{P}_g = \bar{x}^* + \int_{\bar{x}^*}^1 \frac{1}{k_{rg}} d\hat{x} \quad [39]$$

Results and Discussion

In the following, we plot the 1D analytical solutions obtained in the preceding section. Uniform local current density I and net water transport coefficient α are considered. These two factors usually depend on the local electrochemical kinetics and mass transport within the membrane electrode assembly (MEA) and vary along the channel. Assuming uniform distributions of these two parameters is necessary as the MEA mechanisms are excluded in this study. The assumption also facilitates the investigation, i.e., the observed channel phenomena are solely attributed to two-phase transport characteristics. Also in the following discussion, we focus on a standard operating condition, a cell temperature of 80°C, and RH ranging from 25 to 100%, as well as typical cell channel dimensions (see Table I).

Figure 3 shows the gas-phase velocity profiles within the channel at different RHs, calculated from Eq. 19 and 31. The apexes are the transition locations from single- to two-phase flows. The gas velocity increases along the channel during the first stage (single-phase flow) then decreases in the two-phase region. The increasing trend in the single-phase region is due to a mass source by the reaction and transport added to the gas-phase flow. The increment along the chan-

Table I. Geometrical, physical, and operating parameters.

Quantity	Value
Gas channel depth/width/length	1.0/1.0/100 mm
Average current density, I_{av}	1.0 A/cm^2
Temperature of fuel cell, T	353.15 K
Viscosity of liquid water, μ_l [7,24]	3.5×10^{-4} kg/m s
Permeability of the porous-media channel, K [26]	3×10^{-9} m^2
Net water transport coefficient α [27]	0.1
Surface tension, liquid-water–air (80°C), σ [7,24]	0.0625 N/m
Contact angle of the channel wall, θ_c	120°
Stoichiometric flow ratio, ξ	2.0

nel is small, <5%. When liquid emerges, the mass addition is mostly into the liquid phase, as the gas one is already saturated. The oxygen consumption withdraws the mass from the reactant gas, leading to decreasing gas velocities. The decelerating gas flow and oxygen consumption induce a water-phase change from vapor to liquid, further reducing the gas mass flow rate. Furthermore, we find the overall variation in the gas velocity along the channel small (<10%) in most cases. This variation decreases when increasing the value of RH at the low RH region, while it increases with the RH at the high RH one, as indicated in this figure.

Figure 4 shows the profiles of the water concentration in the gas phase. As the gas-phase velocity variation is small, the water concentration increases nearly linearly along the channel in the single-phase region. This is partly due to the uniform current density and net water transport coefficient considered. In real cases, these two factors vary spatially; one can then use Eq. 23 to obtain the water profile. The small deviation from the linear trend observed in this figure (e.g., see the case of RH = 25%) arises primarily from the gas flow change that is shown in Fig. 3. Once reaching the saturation level, water concentration remains constant due to the equilibrium between the gas and liquid phases in the porous-media channel.

Figure 5 displays the profiles of superficial liquid-phase velocity within the channel. In the single-phase region, the liquid velocity is zero, while it increases almost linearly along the channel in a two-phase region. Also, the higher the RH is, the earlier the liquid appears in the channel and also the higher the liquid velocity is at the outlet. The magnitude of the superficial velocity is approximately 10^{-4} m/s. Considering high porosity (~0.95) and the channel

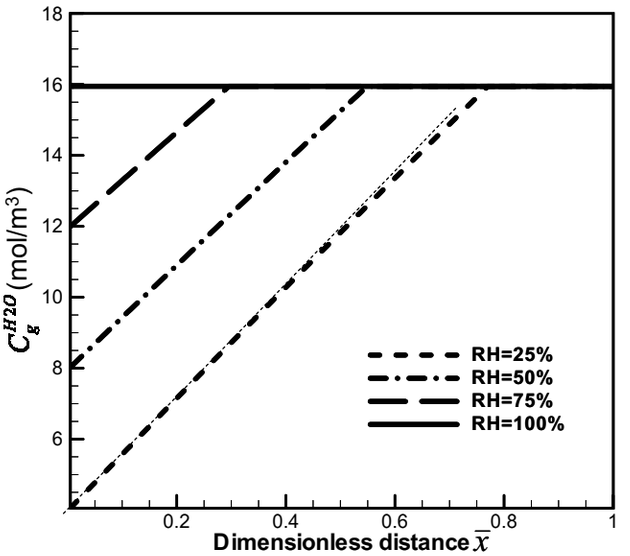

Figure 4. Profiles of the water vapor concentration along the channel at different values of RH. The thin dashed line near the curve of RH = 25% indicates the linear trend.

length (~0.1 m), the time constant of liquid water transport is approximately 1000 s, which is much larger than other dynamic processes observed in fuel cells such as the membrane hydration,[34] GDL dehydration,[15] and cold start.[28]

Figure 6 shows the liquid water saturation profiles for the four cases using the explicit solution of Eq. 35, which neglects the impact of the capillary action on the channel transport along the channel. Liquid builds up quickly along the channel right after it emerges, and then the saturation increase slows down. Therefore, even for the lowest RH, the liquid saturation can still reach around 15% near the outlet, while for an RH of 100%, the liquid saturation is approximately 20%. This can be explained by the fact that the effective permeability of liquid is small at low saturation and increases rapidly with saturation (see Eq. 6 with $n_k = 4$). Therefore, at low saturation, the relative permeability of the liquid phase is very small, leading to local liquid accumulation. As the liquid saturation becomes larger, the relative permeability increases rapidly and en-

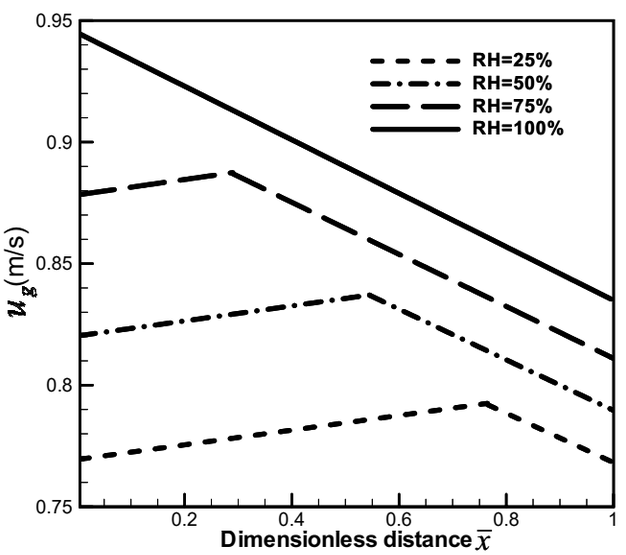

Figure 3. Profiles of the gas-phase superficial velocity in the channel at different values of RH.

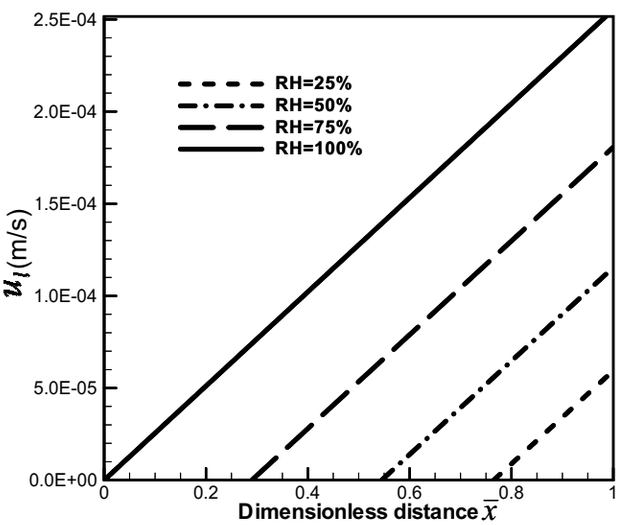

Figure 5. Profiles of the liquid water superficial velocities along the channel at different values of RH.

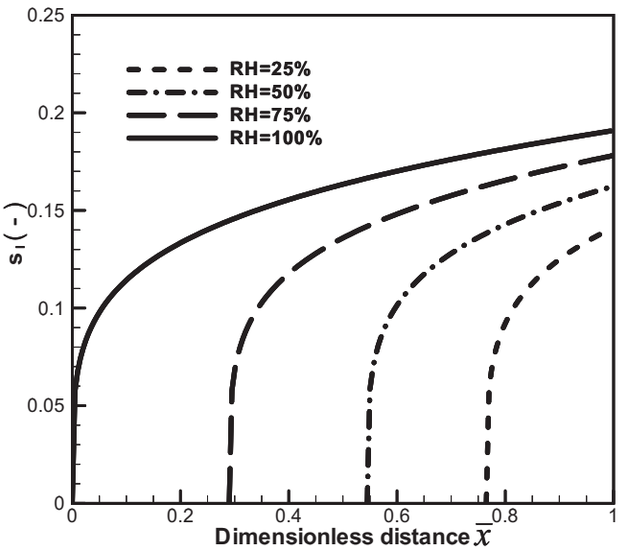

Figure 6. Liquid water saturation profiles along the channel for different values of RH predicted by Eq. 35 using Eq. 6 for the relative permeability ($n_k = 4$).

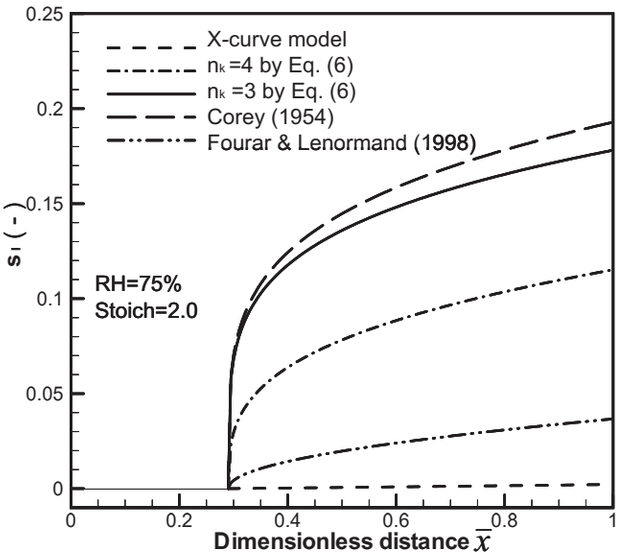

Figure 8. Liquid water profiles using different models for the relative permeability.

hances the liquid water transport in the channel. The significance of this saturation result is that this porous-media channel leads to a modest saturation of ~20% within the channel, avoiding a large resistance for gas reactant transport. Further, due to the dominant interfacial force, the pores always contain liquid and gas phases, alleviating the concerns of the two-phase transition in the traditional hollow channel configuration, e.g., from the annulus flow to slug.[3] The slug flow completely blocks oxygen transport in parts of the channels, leading to local reactant starvation. Insufficient reactant supply reduces cell performance and durability.

The results in the previous figure are obtained from Eq. 35, which neglects the capillary action. Figure 7 includes this capillary effect and is obtained through numerically solving the first-order ordinary differential equation (Eq. 34). Also in Fig. 7, the curves predicted by Eq. 35 are included to compare with the one by Eq. 34. The two equations give almost exactly the same results. Only a small difference can be observed, as shown in the close-up window. Therefore, the capillary mechanism can be safely neglected when analyzing the channel two-phase transport along the channel. Our extensive parametric study also indicates that this conclusion can be applied to channels with different wettabilities. However, the capillary mechanisms may play an important role in liquid transport in the through- or in-plane directions, which is beyond this study's scope.

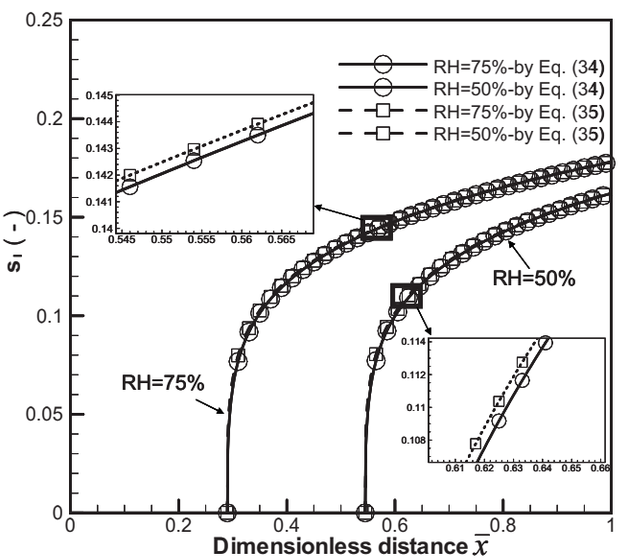

Figure 7. Liquid water profiles predicted by Eq. 34 and 35 using Eq. 6 for the relative permeability ($n_k = 4$).

The relative permeabilities play an important role in phase transport along the channel. Figure 8 plots the saturation profiles at RH = 75% using different expressions of the permeabilities. The prediction depends on the model of the relative permeability adopted. The maximum liquid saturation varies from around 1–20%. In particular, the *X*-curve model gives the smallest fraction of liquid water in the two-phase region, <1%. Others give similar trends but in different magnitudes. The relative permeability of Fourar and Lenormand[30] shows a prediction lower than 5%, while that of Corey[32] leads to a profile higher than Eq. 6 with $n_k = 4$. Corey[32] gave the same liquid relative permeability as Eq. 6 but a different gas relative one. This distinction is responsible for the difference in the liquid saturation predictions by these two expressions.

Figure 9 displays the gas pressure profiles within the channel predicted by Eq. 24 and 36 using the relative permeability of Eq. 6 at $n_k = 4$. Corresponding to Fig. 3, this figure clearly shows two trends of pressure change along the channel: The first stage is the pressure drop in the single-phase region; the other is the gas pressure drop in the two-phase one. Both trends are almost linear but different in slope. The two-phase region displays a more rapid decline in the gas pressure despite the decreasing gas velocity, as shown in Fig. 3. This can be explained by the presence of liquid water, which narrows the passage of the gas flow. A slight difference in pressure curves is observed in the single-phase region among the three cases, which can be explained by the fact that inlet flow rates at fixed stoichiometry differ at varying RHs due to water vapor dilution.

As seen from the previous figure, the gas pressure drops faster in the two-phase region. The RH is an important factor determining the emerging site and saturation level of the two-phase region (see Fig. 6). The gas pressure drop through the channel as a function of RHs is quantified by Eq. 38 and approximated by Eq. 39, which is plotted in Fig. 10. This figure displays the dimensionless pressure drops at varying RHs using Eq. 6 for the relative permeability. The dimensionless pressure drop increases with the RH as the two-phase re-

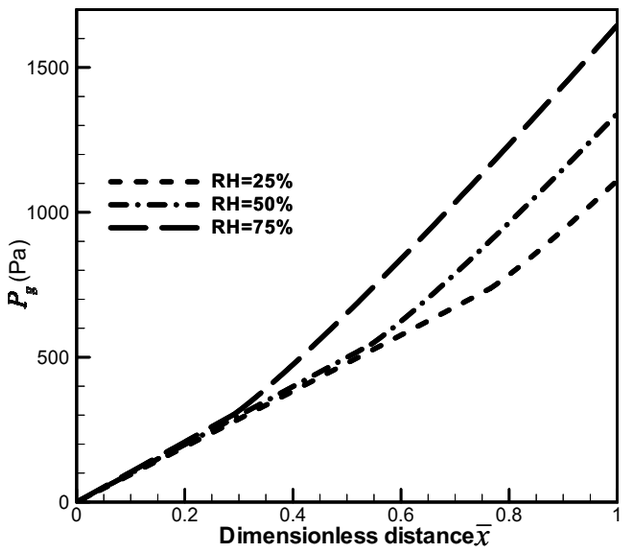

Figure 9. Gas pressure profiles within the channels for different values of RH.

gion becomes larger at higher RHs. This drop is also related to the two-phase interaction. The relative permeability k_{rg} is a key parameter that quantifies the interaction, i.e., the degree of liquid affecting the gas flow. Therefore, a smaller exponent, i.e., $n_k = 3$, shows a much lower pressure drop. Further, a simpler expression of the dimensionless pressure drop is provided by Eq. 39, which assumes a constant gas velocity along the channel. Equation 39 is also plotted in Fig. 10 for comparison, which shows similar trends as Eq. 38. Small deviations are observed at low RHs (Eq. 39 underestimates the pressure drop), while at high RHs, its prediction is higher. But both predictions are close within a 10% difference.

Conclusions

In this study, we developed a two-fluid model for the flow within the porous-media channel of a PEFC to investigate the characteristics of a channel two-phase flow. We further conducted a 1D analysis and obtained analytical solutions for the profiles of the gas/liquid superficial velocity, two-phase pressures, and liquid water saturation along the channel. We found that the superficial gas velocity changes differently between single and two-phase regions. In most cases, the predicted saturation was found to increase rapidly right after the emerging site, followed by a slower increasing pace. The influence of the capillary action on liquid transport along the channel is negligibly small. We also found that the proposed channel configuration results in a modest flooding for all considered cases (the liquid saturation $<20\%$). The dimensionless overall gas pressure drop increases rapidly with RHs, and the prediction highly depends on the model of the relative permeability adopted.

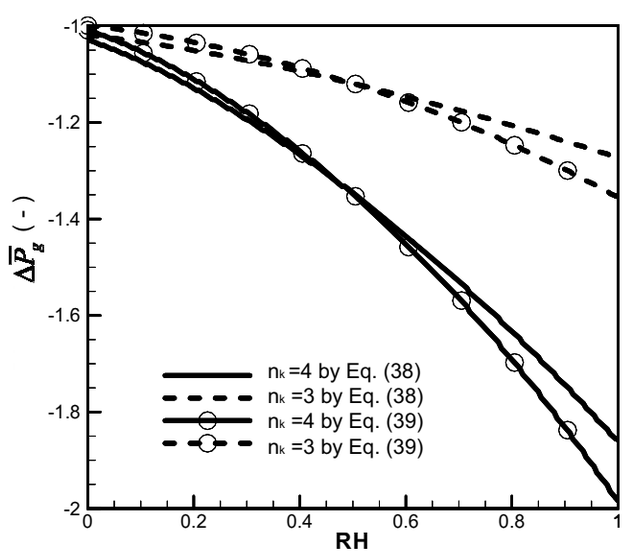

Figure 10. Dimensionless pressure drop as a function of the RH.

Acknowledgments

Partial support of this work by the Academic Senate Council on Research, Computing and Library Resources at UCI is gratefully acknowledged. The author also thanks Kevin Ni from Whitney High School, Cerritos, CA, for help with the two-phase flow visualization.

The University of California, Irvine assisted in meeting the publication costs of this article.

List of Symbols

A	area, m^2
C	molar concentration, mol/m^3
D	mass diffusivity of species, m^2/s
F	Faraday's constant, 96,487 C/equivalent
I	current density, A/cm^2
k_r	relative permeability
K	permeability, m^2
L	length, m
M	molecular weight, kg/mol
N	the direction normal to the surface
P	pressure, Pa
R	gas constant, 8.134 J/mol K
s	liquid saturation
S	source term in transport equations

Stoichiometric ratio

t	time, s
T	temperature, K
$\mathbf{u}$	velocity vector, m/s

Greek

α	net water transport coefficient per proton
ε	porosity
υ	kinematic viscosity, m^2/s
ξ	stoichiometric flow ratio
ρ	density, kg/m^3
σ	surface tension, N/m

Superscripts and subscripts

av	average
c	cathode
g	gas phase
l	liquid phase
m	membrane or mass
in	inlet
sat	saturate value

References

1. K. Tüber, D. Pócza, and C. Hebling, *J. Power Sources*, **124**, 403 (2003).
2. X. G. Yang, F. Y. Zhang, A. Lubawy, and C. Y. Wang, *Electrochem. Solid-State Lett.*, **7**, A408 (2004).
3. F. Y. Zhang, X. G. Yang, and C. Y. Wang, *J. Electrochem. Soc.*, **153**, A225 (2006).
4. Y. Wang, C. Y. Wang, and K. S. Chen, *Electrochim. Acta*, **52**, 3965 (2007).
5. Z. H. Wang, C. Y. Wang, and K. S. Chen, *J. Power Sources*, **94**, 40 (2001).
6. J.-H. Nam and M. Kaviany, *Int. J. Heat Mass Transfer*, **46**, 4595 (2003).
7. U. Pasaogullari and C. Y. Wang, *J. Electrochem. Soc.*, **151**, A399 (2004).
8. D. Natarajan and T. V. Nguyen, *J. Electrochem. Soc.*, **148**, A1324 (2001).
9. S. Mazumder and J. V. Cole, *J. Electrochem. Soc.*, **150**, A1510 (2003).
10. A. Z. Weber and J. Newman, *J. Electrochem. Soc.*, **152**, A677 (2005).
11. U. Pasaogullari and C. Y. Wang, *J. Electrochem. Soc.*, **152**, A380 (2005).
12. E. Birgersson, M. Noponen, and M. Vynnycky, *J. Electrochem. Soc.*, **152**, A1021 (2005).
13. H. Meng and C. Y. Wang, *J. Electrochem. Soc.*, **152**, A1733 (2005).
14. Y. Wang and C. Y. Wang, *J. Electrochem. Soc.*, **153**, A1193 (2006).
15. Y. Wang and C. Y. Wang, *J. Electrochem. Soc.*, **154**, B636 (2007).

16. A. Rowe and X. Li, *J. Power Sources*, **102**, 82 (2001).
17. L. You and H. Liu, *Int. J. Heat Mass Transfer*, **45**, 2277 (2002).
18. J. Yuan and B. Sunden, *Electrochim. Acta*, **50**, 677 (2004).
19. P. Costamagna, *Chem. Eng. Sci.*, **56**, 323 (2001).
20. T. Berning and N. Djlali, *J. Electrochem. Soc.*, **150**, A1589 (2003).
21. C. Y. Wang and P. Cheng, *Adv. Heat Transfer*, **30**, 93 (1997).
22. M. Hu, A. Gu, M. Wang, X. Zhu, and L. Yu, *Energy Convers. Manage.*, **45**, 1861 (2004).
23. G. Luo, H. Ju, and C. Y. Wang, *J. Electrochem. Soc.*, **154**, B316 (2007).
24. Y. Wang, *J. Power Sources*, **185**, 261 (2008).
25. Y. Wang and X. H. Feng, *J. Electrochem. Soc.*, **155**, B1289 (2008).
26. Y. Wang, S. Basu, and C. Y. Wang, *J. Power Sources*, **179**, 603 (2008).
27. Y. Wang, *J. Electrochem. Soc.*, **156**, B1124 (2009).
28. Y. Wang, *J. Electrochem. Soc.*, **154**, B1041 (2007).
29. R. Hilfer, *Phys. Rev. E*, **58**, 2090 (1998).
30. M. Fourar and R. Lenormand, Paper SPE 49006 presented at the SPE Annual Technical Conference and Exhibition, New Orleans, LA, 1998.
31. A. T. Corey, *Mechanics of Immiscible Fluids in Porous Media*, 2nd ed., Water Resources (1986).
32. A. T. Corey, *Producers Monthly*, **19**, 38 (1954).
33. N. Speyer, K. Li, and R. Horne, in *Proceedings of the 32nd Workshop on Geothermal Reservoir Engineering*, Stanford University, Stanford, CA, Paper no. SGP-TR-183 (2007).
34. Y. Wang and C. Y. Wang, *Electrochim. Acta*, **50**, 1307 (2005).